

**Anisotropic properties of a noncentrosymmetric NbReSi superconducting single crystal**Suman Nandi , Souvik Sasmal , Bishal Baran Maity , Vikash Sharma, Gourav Dwari ,  
Ruta Kulkarni, and A. Thamizhavel \**Department of Condensed Matter Physics and Materials Science, Tata Institute of Fundamental Research, Homi Bhabha Road, Colaba, Mumbai 400005, India*

(Received 27 November 2022; accepted 7 April 2023; published 25 April 2023)

A single crystal of NbReSi which crystallizes in the hexagonal structure with the noncentrosymmetric space group  $P62m$  (No. 189) has been grown by the Czochralski method using a tetra-arc furnace. The anisotropic physical properties have been studied by measuring the magnetic susceptibility and electrical transport. The superconducting transition temperature ( $T_c$ ) is around 6.1 K, and the measured upper critical field ( $H_{c2}$ ) values are 8.39 T and 11.65 T for applied field parallel to  $[0001]$  and  $[11\bar{2}0]$ , respectively. The anisotropy ratio  $\Gamma = H_{c2}^a/H_{c2}^c$  is close to 1.38. The GL parameters  $\kappa_c$  and  $\kappa_a$  are much larger than  $1/\sqrt{2}$ , indicating that NbReSi is a strong type-II superconductor. The lower critical field ( $H_{c1}$ ) values are very small (1.65 mT for  $H \parallel [0001]$  and 1.22 mT for  $H \parallel [11\bar{2}0]$ ) compared to  $H_{c2}$ . From the magnetization hysteresis loops, calculated critical current at low field is of the order  $10^4$  A/cm<sup>2</sup> which indicates the presence of strong pinning in the sample.

DOI: [10.1103/PhysRevB.107.134518](https://doi.org/10.1103/PhysRevB.107.134518)**I. INTRODUCTION**

A noncentrosymmetric material has a crystal structure where a center of inversion is absent, which leads to an internal electric field gradient resulting in the various interesting physical properties. Research on noncentrosymmetric superconductors (NCSCs) [1] got intensified after the discovery of heavy fermion superconductivity and antiferromagnetism in noncentrosymmetric CePt<sub>3</sub>Si [2]. The main ingredient for understanding the physics of noncentrosymmetric superconductors is the Rashba type antisymmetric spin-orbit coupling (ASOC), which can lift the spin degeneracy of the electronic bands and induce pairing of spin-singlet and spin-triplet states [3,4]. Such things can exhibit many unconventional features like unusual magnetic properties, high upper critical field exceeding the Pauli limiting field [5], nodes in the energy gap [6,7], and presence of Majorana quasiparticles [8,9], etc. In contrast to the centrosymmetric superconductors, triplet component may exist in a fully spatially symmetric paired state (triplet *s*-wave) due to lack of inversion center [10]. The NCSCs have been found in a variety of compounds, including heavy fermion compounds with strong electron correlation such as CePt<sub>3</sub>Si, CeIrSi<sub>3</sub>, CeCoGe<sub>3</sub>, and CeRhSi<sub>3</sub> [11–14], and weakly correlated materials like Mo<sub>3</sub>Al<sub>2</sub>C [15] and Mg<sub>10</sub>Ir<sub>19</sub>B<sub>16</sub>. Currently researchers pay attention to topological systems which also exhibit superconductivity, e.g., TaOsSi, YPtBi, PbTaSe<sub>2</sub>, and PdBi<sub>2</sub>Te<sub>3</sub> [16–20].

The current research in noncentrosymmetric materials focuses on finding new materials with high ASOC and its effect on the superconducting ground state. High ASOC is expected in material containing high atomic number (*Z*) elements as the strength of ASOC is directly proportional to  $Z^2$ . As an example, in Li<sub>2</sub>Pt<sub>3</sub>B Cooper pair is in a spin triplet state,

whereas Li<sub>2</sub>Pd<sub>3</sub>B is a pure spin singlet *s*-wave superconductor [1,21,22].

Time reversal symmetry (TRS) plays an important role in determining the nature of superconducting ground states. In TRS breaking superconductors, extremely small spontaneous magnetic fields exist in the superconducting ground state due to nonzero moments of the Cooper pairs. This is a rare phenomenon of NCSCs and LaNiC<sub>2</sub>, La<sub>7</sub>Ir<sub>3</sub>, and Zr<sub>3</sub>Ir [23–25] are some examples.

Now a variety of equiatomic silicides MM'Si (M=Nb, Ta; M'=Re, Os, Pt) [26] have been found which exhibit superconductivity at low temperatures. Recently, the existence of superconductivity in noncentrosymmetric polycrystalline NbReSi has been reported [27–29]. The previous studies show the upper critical field ( $H_{c2}$ ) values are above the Pauli limiting field. But in the similar compound TaReSi,  $H_{c2}$  is well below the limit [30]. Further, transverse field muon spin rotation ( $\mu$ SR) measurement confirmed a BCS-type isotropic superconducting gap with  $\Delta(0)/k_B T_c = 1.73$ , indicating disorder or nonmagnetic impurities may increase the value of  $H_{c2}$  [28]. So it is highly recommended to study on single crystals to explore the reason behind enhancement of  $H_{c2}$ . Finally, a band splitting along the *c* axis is observed in DFT calculations which suggests a possible anisotropy in NbReSi [27]. In this manuscript, we report the successful growth of a NbReSi single crystal and report the anisotropic physical properties.

**II. EXPERIMENTAL METHODS**

A single crystal of NbReSi has been grown by the Czochralski method in a tetra-arc furnace. At first, a polycrystalline ingot is prepared from high purity initial elements of Nb (99.99%; Alfa Aesar), Re (99.99%; Alfa Aesar), and Si (99.99%; Alfa Aesar) in the molar ratio 1:1:1.1 by arc melting in argon atmosphere. Here a little excess of Si is essential to compensate the evaporation of Si during growth. The ingot

\*thamizh@tifr.res.in

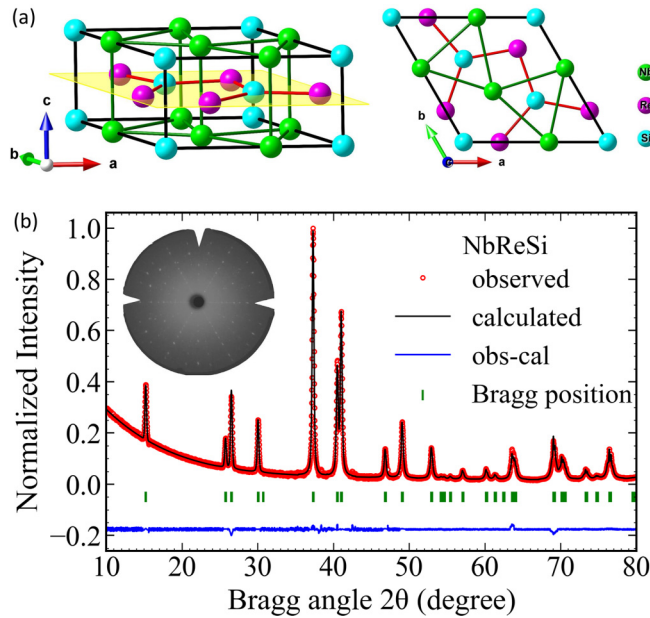


FIG. 1. (a) Crystal structure of NbReSi. (b) Room temperature powder x-ray diffraction pattern of crushed single crystals. Inset shows Laue diffraction pattern corresponding to the (0001) plane.

is flipped and remelted three times for better homogeneity. A seed is cut from this ingot to grow the single crystal. After melting the ingot, the seed is carefully brought down close to the melt. Once the turbulence in the melt is minimum such that the sample is just above the melting point, the seed rod is inserted into the melt and immediately pulled rapidly at a rate of 100 mm/h. After the necking process and achieving the steady state condition, the pulling speed is reduced to 10 mm/h and the growth is continued for almost 8 hours. Finally, we obtain an 8 to 9 cm long crystal with an average diameter of 3 mm. The stoichiometry of the crystal as determined from the energy dispersive analysis by x-ray (EDAX) is Nb : Re : Si = 1 : 0.99 : 1.05 [31]. Powder x-ray and Laue diffraction experiments are performed to determine phase purity and crystallographic orientation. Two samples are cut along  $[11\bar{2}0]$  ( $ab$  plane) and  $[0001]$  ( $c$  axis) directions using a wire electric discharge machine (EDM) for transport and magnetic measurements. The magnetization measurements are carried out using vibrating sample magnetometer (VSM) and electrical resistivity measurements are done in a physical properties measurement system (PPMS), Quantum Design, USA equipped with a 14 T magnet.

### III. RESULTS AND DISCUSSION

#### A. X-ray diffraction

NbReSi crystallizes in the ZrNiAl-type hexagonal structure with the space group  $P6_2m$  (189). Figure 1(a) illustrates the crystal structure of NbReSi. In the unit cell, Nb and Re atoms occupy  $3f$  and  $3g$  Wyckoff's position, while Si atoms occupy  $2d$  and  $1a$  sites. To check the phase purity, a small part of grown crystal is crushed to fine powder. The XRD measurement is performed in PANalytical x-ray diffractometer using monochromatic source of Cu  $K_\alpha$  with wavelength

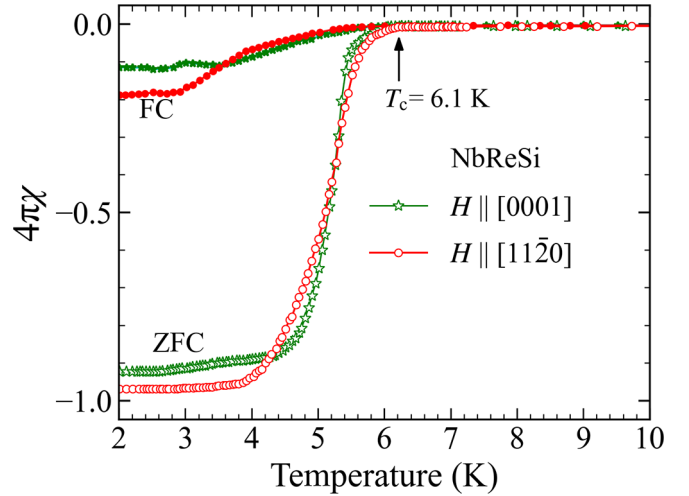


FIG. 2. Temperature dependence of low field ( $H = 0.5$  mT) magnetic susceptibility for  $H \parallel [11\bar{2}0]$  and  $[0001]$  using both ZFC and FC protocols.

$\lambda = 1.5406$  Å. Figure 1(b) shows the powder pattern at 300 K with the Bragg angle  $2\theta$  scan ranging from  $10^\circ$  to  $80^\circ$ . Using Rietveld analysis with FULLPROF software [33], we confirmed that the grown crystal is phase pure and crystallizes in the hexagonal crystal structure. The estimated lattice parameters  $a = 6.717$  Å and  $c = 3.457$  Å are consistent with the previous reports [27].  $[11\bar{2}0]$  and  $[0001]$  directions are identified by Laue diffraction in the back reflection geometry which is shown in the inset of Fig. 1(b).

#### B. Magnetic properties

The temperature dependence of dc magnetic susceptibility  $\chi(T)$  measured in a field of 0.5 mT along  $[11\bar{2}0]$  and  $[0001]$  under zero-field-cooled (ZFC) and field-cooled (FC) processes, is shown in Fig. 2. The onset of the superconducting state in NbReSi is observed at  $T_c^{\text{onset}} = 6.1$  K which is slightly low compared to the previous reports [27,29]. There are large differences between the FC and ZFC susceptibilities because vortices are pinned during FC condition. Superconducting volume fraction at low temperature (2 K) in the ZFC data for fields applied along both crystallographic directions is  $\sim 1$  which indicates bulk superconductivity in the sample.

In order to investigate the field dependence of the  $M$ - $T$  curves, the magnetization measurements are carried out in different fields ranging from 0.5 mT to 10 T. Superconducting transition temperature is suppressed with increasing magnetic field for both directions (Fig. 3).

The insets of Figs. 4(a) and 4(b) show the field dependent magnetization  $M(H)$  for various temperatures up to  $T_c$  using ZFC protocol after accounting for the demagnetization factor. To minimize the demagnetization effect we have applied field along the long side of the crystal. For each temperature,  $H_{c1}$  is determined as the value where  $M(H)$  deviates from linearity.

To get the value of  $H_{c1}$  at 0 K, we have fitted the data with the Ginzburg-Landau (GL) relation [34]

$$H_{c1}(T) = H_{c1}(0) \left[ 1 - \left( \frac{T}{T_c} \right)^2 \right], \quad (1)$$

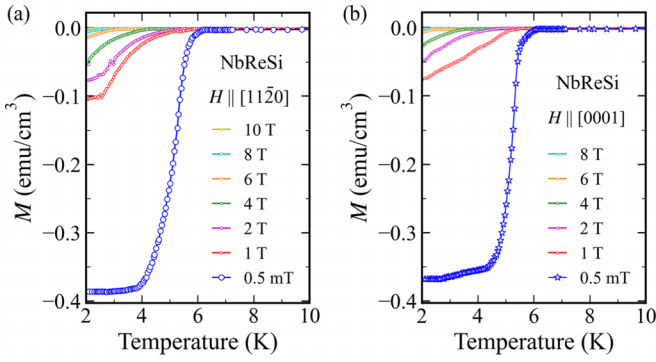


FIG. 3. Variation of magnetization with temperature for different magnetic fields along (a)  $[11\bar{2}0]$  and (b)  $[0001]$  directions.

which results in a value of  $H_{c1}^a(0) = 1.22 \pm 0.01$  mT and  $H_{c1}^c(0) = 1.65 \pm 0.03$  mT for the two principal crystallographic directions. This indicates the anisotropy in the superfluid density.

Magnetic hysteresis loops are observed with fields applied both parallel to  $[0001]$  and  $[11\bar{2}0]$  directions at 2 K. The loops provide evidence that NbReSi is a type II superconductor with strong vortex pinning. The type II superconductivity is also indicated by previous studies with polycrystalline samples [27,28]. From Fig. 5(a), the irreversible field is about 10 T for  $H \parallel [11\bar{2}0]$  and 7.5 T for  $H \parallel [0001]$ . This anisotropic behavior indicates that vortex pinning for  $H \parallel [11\bar{2}0]$  is stronger than that for  $H \parallel [0001]$ . We can calculate critical current density  $J_c^{x,y}$  ( $x$  and  $y$  refer to the direction of current and magnetic field) using Bean's model [35,36]:

$$J_c = \frac{20\Delta M}{w(1-w/3l)}, \quad (2)$$

where  $\Delta M$  is width of the hysteresis loop.  $w$  and  $l$  are sample width and length ( $l > w$ ) for a particular field orientation. Here all lengths are in cm,  $M$  is in  $\text{emu}/\text{cm}^3$ , and current density is in  $\text{A}/\text{cm}^2$ . When magnetic field is along the  $c$  axis, supercurrent density is generated by vortices perpendicular to the  $ab$  plane. From Fig. 5(b) at 2 K,  $J_c^{ab,c}$  reaches a high value of  $8714 \text{ A}/\text{cm}^2$  and decreases with increasing magnetic

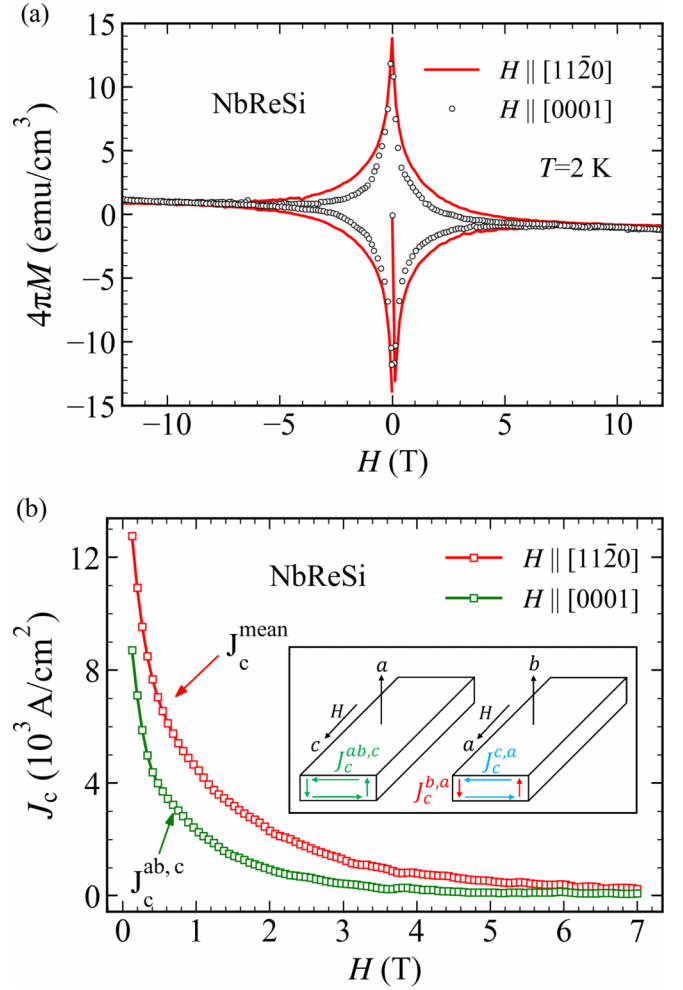


FIG. 5. (a) Magnetic hysteresis loop, (b) critical current density  $J_c$ ; Inset: Components of critical current density for both field directions.

field. But the situation is more complicated when magnetic field is parallel to the  $ab$  plane because there are two current densities  $J_c^{b,a}$  and  $J_c^{c,a}$  in two different directions. If we assume

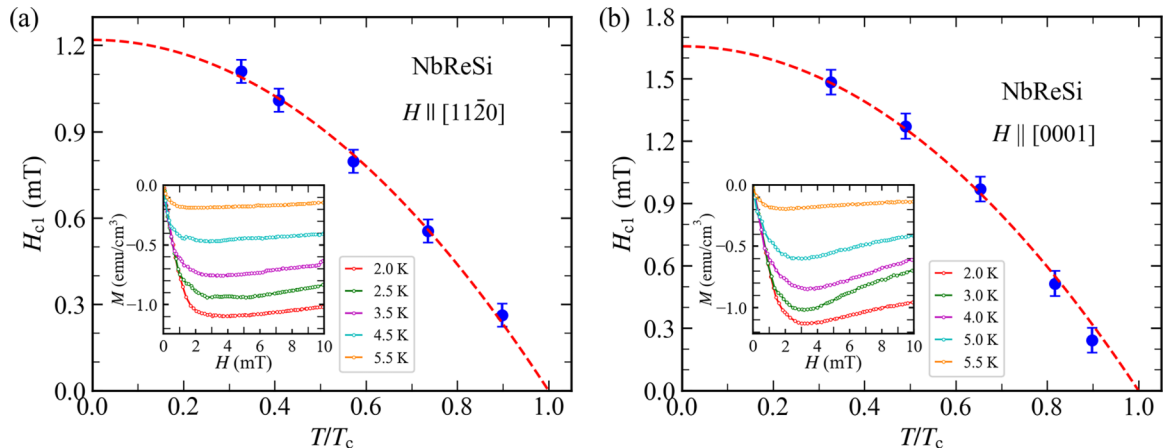


FIG. 4. Lower critical fields  $H_{c1}$  vs temperature. Dashed line is a fit to GL equation; Inset: Field dependent magnetization measured at different temperatures.

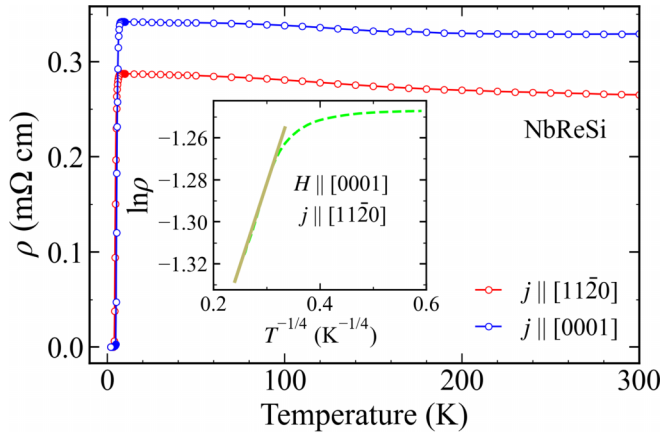


FIG. 6. Temperature dependence of resistivity for current parallel to  $[11\bar{2}0]$  and  $[0001]$  directions; Inset shows the  $\ln\rho$  as a function of  $T^{-1/4}$  for  $j \parallel [11\bar{2}0]$ . Solid line is the fitting of the 3D variable range hopping (VRH) model to the data in the range of 100 to 300 K.

$J_c^{b,a} = J_c^{c,a}$ , weighted average  $J_c^{\text{mean}}$  can be calculated using Eq. (2) which exceeds  $10^4$  A/cm<sup>2</sup>. Variation of  $J_c^{ab,c}$  and  $J_c^{\text{mean}}$  with magnetic field up to 7 T is shown in Fig. 5(b).

### C. Electrical Resistivity

To measure resistivity we have made electrical contacts using a conventional four-probe method with 50  $\mu\text{m}$  gold wire. Figure 6 shows the temperature dependence of resistivity along both the principle directions  $[11\bar{2}0]$  and  $[0001]$  of a NbReSi single crystal in a zero magnetic field. At 300 K, the resistivity is anisotropic reflecting hexagonal crystal structure. It is evident from Fig. 6 that NbReSi is a poor metal. The resistivity weakly increases during cooling from 300 K to 7 K along both the directions. This result contradicts the previously reported polycrystalline data where a pure metallic behavior is shown in this temperature range [27]. As confirmed by the EDAX, a slightly off-stoichiometric nature may be the reason for variance in the electrical resistivity behavior from that of the polycrystalline samples. Then resistivity suddenly drops to zero indicating a superconducting transition. In a temperature range from 300 K to 100 K, bad-metal behavior

can be described by the three-dimensional (3D) variable range hopping (VRH) model [37]

$$\rho(T) = \rho_0 \exp\left[\left(\frac{T_0}{T}\right)^{1/4}\right], \quad (3)$$

where  $T_0 = \frac{\beta}{kg(\mu)r^3}$ ,  $g(\mu)$  is density of states at Fermi level,  $r$  is localization radius of states near the Fermi level, and  $\beta$  is a numerical coefficient. The inset of Fig. 6 describes this very well. From the fit we obtain  $\rho_0 = 0.22$  m $\Omega$  cm and  $T_0 = 3.1$  K. When the temperature is below 100 K, the resistivity deviates drastically from the 3D VRH model. This feature is similar to members of the RPdBi series [38,39].

To study the superconducting anisotropy, resistivity measurements with applied magnetic field along the two principle crystallographic directions are performed. Figures 7(a) and 7(b) show resistivity measurements up to 10 T for current parallel to the  $c$  axis and  $ab$  plane, respectively. In both cases, the field was perpendicular to the current. The superconducting transitions are gradually suppressed to lower temperatures and become broader with the increase in magnetic field. The temperature dependence of upper critical field  $H_{c2}$  is determined from the resistivity data. As the transition is a little broad, we have defined the transition temperature as temperature where the resistivity is 90% of  $\rho_n$  (normal state resistivity). We have used the phenomenological Ginzburg-Landau (GL) expression [34]

$$H_{c2}(T) = H_{c2}(0) \left[ \frac{1-t^2}{1+t^2} \right], \quad \text{where } t = \frac{T}{T_c} \quad (4)$$

to obtain  $H_{c2}(0)$ . An extrapolation to  $T = 0$  using this model has yielded  $H_{c2}^a(0) = 11.6 \pm 0.2$  T and  $H_{c2}^c(0) = 8.4 \pm 0.1$  T. The Pauli limiting field  $H_{c2}^p(0) = 1.86T_c = 11.34$  T is comparable to  $H_{c2}^a(0)$  but larger than  $H_{c2}^c(0)$ . Here spin-orbit coupling may have an influence on the value of  $H_{c2}$  because of heavier elements in the system. So we fit the data using the Werthamer-Helfand-Hohenberg (WHH) model [40,41], which calculate  $H_{c2}(T)$  taking into account both spin-orbit coupling and Pauli spin paramagnetism. The WHH theory

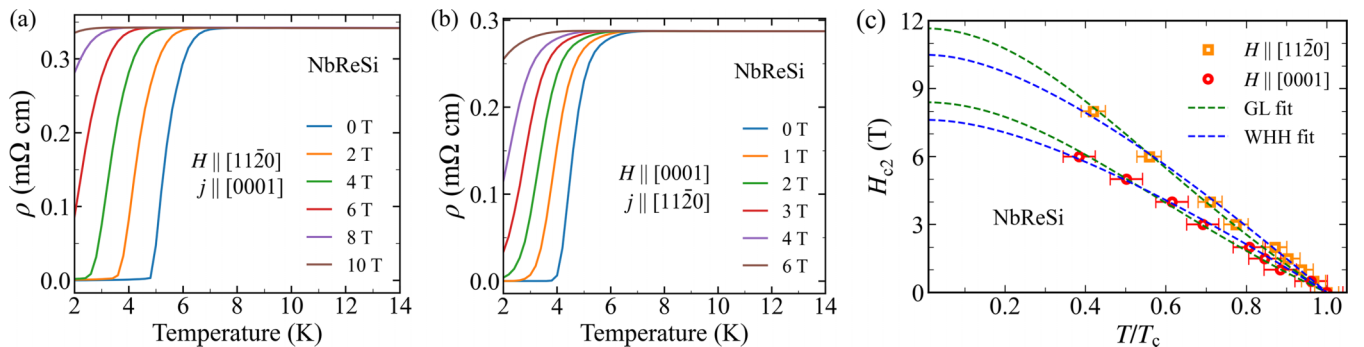


FIG. 7. Variation of resistivity with temperature for different magnetic field along (a)  $[11\bar{2}0]$  direction and (b)  $[0001]$  direction. (c) Upper critical field as a function of temperature for NbReSi where the  $H_{c2}(T)$  points are extracted from the  $T_c$  in electrical resistivity. Fits using the WHH and GL models are shown by the dashed lines.

TABLE I. Parameters obtained from WHH fit.

	$\alpha$	$\lambda_{so}$	$H_{c2}$ (T)
$H \parallel [11\bar{2}0]$	1.32	15	10.5
$H \parallel [0001]$	1.13	20	7.6

gives

$$\begin{aligned} \ln\left(\frac{1}{t}\right) &= \left(\frac{1}{2} + \frac{i\lambda_{so}}{4\gamma}\right) \psi\left(\frac{1}{2} + \frac{h + \frac{1}{2}\lambda_{so} + i\gamma}{2t}\right) \\ &+ \left(\frac{1}{2} - \frac{i\lambda_{so}}{4\gamma}\right) \psi\left(\frac{1}{2} + \frac{h + \frac{1}{2}\lambda_{so} - i\gamma}{2t}\right) \\ &- \psi\left(\frac{1}{2}\right), \end{aligned} \quad (5)$$

where  $t = \frac{T}{T_c}$ ,

$$h = 2eH_{c2}v_f^2\tau_{tr}/6\pi k_B T_c,$$

$$\gamma = \left[ (\alpha h)^2 - \left(\frac{1}{2}\lambda_{so}\right)^2 \right]^{\frac{1}{2}},$$

$$\alpha = 3\hbar/2mv_f^2\tau_{tr},$$

$\lambda_{so}$  is the spin-orbit coupling parameter, and  $\alpha$  is the Maki parameter. After fitting the data to this model, obtained parameters are listed in Table I. High values of  $\lambda_{so}$  indicate the presence of significant amount of spin orbit coupling. Although we estimated the  $H_{c2}$  by using GL and WHH models, the value obtained from the WHH model is considered to give a better estimate of the  $H_{c2}$  as it included the spin-orbit coupling term. The anisotropy ratio of  $H_{c2}$  is calculated as  $\Gamma(0) = H_{c2}^a(0)/H_{c2}^c(0) = 1.37$  which is almost same as the value got from GL model.

The Ginzburg-Landau (GL) coherence length along the  $i$  direction  $\xi_i$  is estimated from the anisotropic Ginzburg-Landau formulas [42,43] for  $H_{c2}$ :  $H_{c2}^a = \phi_0/(2\pi\xi_a\xi_c)$  and  $H_{c2}^c = \phi_0/(2\pi\xi_a^2)$ , where the flux quantum  $\phi_0 = 2.067 \times 10^{-15}$  Wb. The coherence length values  $\xi_a$  and  $\xi_c$  are  $6.26 \pm 0.04$  nm and  $4.51 \pm 0.05$  nm, respectively, resulting in a ratio of  $\xi_a/\xi_c \approx 1.39$ .

The GL parameter  $\kappa_i(0)$  is related to the coherence length  $\xi_i(0)$  and the GL penetration depth  $\lambda_i(0)$  as  $\kappa_c(0) = \lambda_a(0)/\xi_a(0)$  and  $\kappa_a(0) = \lambda_a(0)/\xi_c(0) = [\lambda_a(0)\lambda_c(0)/\xi_a(0)\xi_c(0)]^{1/2}$ . The anisotropic GL relations require that  $\xi_a/\xi_c = \lambda_c/\lambda_a$ . Lower critical field values can also be used to determine the GL penetration depth  $\lambda_i(0)$ , using the

equation [43]

$$H_{c1}^c(0) = \frac{\phi_0}{4\pi\lambda_a(0)^2} \ln\kappa_c(0) = \frac{\phi_0}{4\pi\lambda_a(0)^2} \ln\frac{\lambda_a(0)}{\xi_a(0)},$$

$$H_{c1}^a(0) = \frac{\phi_0}{4\pi\lambda_a(0)\lambda_c(0)} \ln\kappa_a(0) = \frac{\phi_0}{4\pi\lambda_a(0)\lambda_c(0)} \ln\frac{\lambda_a(0)}{\xi_c(0)}.$$

Calculated penetration depth values  $\lambda_c = 991 \pm 18$  nm and  $\lambda_a = 683 \pm 5$  nm, and their ratio  $\lambda_c/\lambda_a = 991/683 \approx 1.45$ . This is much closer to the ratio of the coherence lengths  $\xi_a/\xi_c$ , as required by the GL theory. The GL parameters  $\kappa_c = 268.8$  and  $\kappa_a = 373.1$  are much larger than  $1/\sqrt{2}$ , indicating that NbReSi is a strong type-II superconductor. Penetration depth  $\lambda_a$  is much smaller than  $\lambda_c$  because the screening currents flow more easily along the NbSi or ReSi planes than in the  $c$  direction. The GL estimation of  $H_{c1}(0)$ ,  $H_{c2}(0)$ ,  $\xi(0)$ ,  $\lambda(0)$ , and  $\kappa(0)$  for both field orientations ( $H \parallel [11\bar{2}0]$  and  $H \parallel [0001]$ ) are given in Table II.

As mentioned in the introduction, in NCSCs, the lifting of the spin degeneracy by ASOC results in the pairing of spin-singlet and spin-triplet states. The general consequence of this admixture of spin-singlet and spin-triplet pairing results in the enhancement of the upper critical field. From our anisotropic investigations on  $H_{c2}(0)$  we have observed that it is less than the Pauli limiting field  $H_{c2}^P(0)$  along both the crystallographic directions in the  $ab$  plane and along the  $c$  axis. The previous studies on the polycrystalline samples have also depicted the upper critical field is almost comparable with that of the Pauli limit. Hence our studies on single crystal NbReSi unequivocally confirm that the paramagnetic limiting is not violated. Furthermore, the recent  $\mu$ SR measurements have revealed that TRS is preserved in NbReSi which indicates the absence of mixed type of pairing, and the nuclear magnetic resonance (NMR) experiments [28,29] confirmed a nodeless superconductivity described by the  $s$ -wave model.

#### IV. CONCLUSION

We have successfully grown a single crystal of NbReSi by the Czochralski method from an off-stoichiometric melt. Powder x-ray diffraction has confirmed the structure and stoichiometry of the grown single crystal, while Laue diffraction patterns depict circular spots, thus confirming a good quality of the single crystal. From resistivity and magnetic susceptibility measurements, NbReSi is confirmed as a type-II superconductor with a transition temperature at 6.1 K. Our studies on the critical fields  $H_{c1}$  and  $H_{c2}$  revealed considerable anisotropy along the two principal crystallographic directions. These anisotropy effects possibly arise due to the significant antisymmetric spin orbit coupling present in the sample. This has been confirmed in the recent band structure calculations by Su *et al.* [27], where they have observed a large band

TABLE II. Characteristic parameters of NbReSi: lower critical field  $H_{c1}(0)$ , upper critical field  $H_{c2}(0)$ , GL coherence length  $\xi(0)$ , GL penetration depth  $\lambda(0)$ , and GL parameter  $\kappa(0)$ .

	$H_{c1}(0)$ (mT)	$H_{c2}(0)$ (T)	$\xi(0)$ (nm)	$\lambda(0)$ (nm)	$\kappa(0)$
$H \parallel [11\bar{2}0]$	$1.22 \pm 0.01$	$11.6 \pm 0.2$	$4.51 \pm 0.05$	$991 \pm 18$	$268.8 \pm 3.7$
$H \parallel [0001]$	$1.65 \pm 0.03$	$8.4 \pm 0.1$	$6.26 \pm 0.04$	$683 \pm 5$	$373.1 \pm 6.8$

splitting along the  $c$  axis related to the high-symmetry lines along the  $\Gamma - A$  and  $M - L$  directions. From our analysis on the  $H_{c2}$ , based on the WHH model; Pauli limiting field is not violated in NbReSi.

## ACKNOWLEDGMENT

We acknowledge the Department of Atomic Energy (DAE), Government of India for financial support.

- [1] M. Smidman, M. B. Salamon, H. Q. Yuan, and D. F. Agterberg, Superconductivity and spin-orbit coupling in non-centrosymmetric materials: a review, *Rep. Prog. Phys.* **80**, 036501 (2017).
- [2] T. Takeuchi, S. Hashimoto, T. Yasuda, H. Shishido, T. Ueda, M. Yamada, Y. Obiraki, M. Shiimoto, H. Kohara, T. Yamamoto, K. Sugiyama, K. Kindo, T. D. Matsuda, Y. Haga, Y. Aoki, H. Sato, R. Settai, and Y. nuki, Magnetism and superconductivity in a heavy-fermion superconductor, CePt<sub>3</sub>Si, *J. Phys.: Condens. Matter* **16**, L333 (2004).
- [3] X. Xu, Y. Li, and C. L. Chien, Spin-Triplet Pairing State Evidenced by Half-Quantum Flux in a Noncentrosymmetric Superconductor, *Phys. Rev. Lett.* **124**, (2020).
- [4] L. P. Gor'kov and E. I. Rashba, Superconducting 2D System with Lifted Spin Degeneracy: Mixed Singlet-Triplet State, *Phys. Rev. Lett.* **87**, 037004 (2001).
- [5] D. A. Mayoh, M. J. Pearce, K. Götze, A. D. Hillier, G. Balakrishnan, and M. R. Lees, Superconductivity and the upper critical field in the chiral noncentrosymmetric superconductor NbRh<sub>2</sub>B<sub>2</sub>, *J. Phys.: Condens. Matter* **31**, 465601 (2019).
- [6] S. Kuroiwa, Y. Saura, J. Akimitsu, M. Hiraishi, M. Miyazaki, K. H. Satoh, S. Takeshita, and R. Kadono, Multigap Superconductivity in Sesquicarbides La<sub>2</sub>C<sub>3</sub> and Y<sub>2</sub>C<sub>3</sub>, *Phys. Rev. Lett.* **100**, 097002 (2008).
- [7] J. Chen, M. B. Salamon, S. Akutagawa, J. Akimitsu, J. Singleton, J. L. Zhang, L. Jiao, and H. Q. Yuan, Evidence of nodal gap structure in the noncentrosymmetric superconductor Y<sub>2</sub>C<sub>3</sub>, *Phys. Rev. B* **83**, 144529 (2011).
- [8] P.-Y. Chang, S. Matsuura, A. P. Schnyder, and S. Ryu, Majorana vortex-bound states in three-dimensional nodal noncentrosymmetric superconductors, *Phys. Rev. B* **90**, 174504 (2014).
- [9] M. Sato and S. Fujimoto, Topological phases of noncentrosymmetric superconductors: Edge states, Majorana fermions, and non-Abelian statistics, *Phys. Rev. B* **79**, 094504 (2009).
- [10] H. Q. Yuan, D. F. Agterberg, N. Hayashi, P. Badica, D. Vandervelde, K. Togano, M. Sigrist, and M. B. Salamon, S-Wave Spin-Triplet Order in Superconductors without Inversion Symmetry: Li<sub>2</sub>Pd<sub>3</sub>B and Li<sub>2</sub>Pt<sub>3</sub>B, *Phys. Rev. Lett.* **97**, 017006 (2006).
- [11] E. Bauer, G. Hilscher, H. Michor, C. Paul, E. W. Scheidt, A. Griбанov, Y. Seropegin, H. Noël, M. Sigrist, and P. Rogl, Heavy Fermion Superconductivity and Magnetic Order in Noncentrosymmetric CePt<sub>3</sub>Si, *Phys. Rev. Lett.* **92**, 027003 (2004).
- [12] N. Metoki, K. Kaneko, T. D. Matsuda, A. Galatanu, T. Takeuchi, S. Hashimoto, T. Ueda, R. Settai, Y. nuki, and N. Bernhoeft, Magnetic structure and the crystal field excitation in heavy-fermion antiferromagnetic superconductor CePt<sub>3</sub>Si, *J. Phys.: Condens. Matter* **16**, L207 (2004).
- [13] Y. Tada, N. Kawakami, and S. Fujimoto, Spin fluctuations and superconductivity in noncentrosymmetric heavy fermion systems CeRhSi<sub>3</sub> and CeIrSi<sub>3</sub>, *Phys. Rev. B* **81**, 104506 (2010).
- [14] R. Settai, Y. Okuda, I. Sugitani, Y. Ōnuki, T. D. Matsuda, Y. Haga, and H. Harima, Non-centrosymmetric heavy fermion superconductivity in CeCoGe<sub>3</sub>, *Int. J. Mod. Phys. B* **21**, 3238 (2007).
- [15] E. Bauer, G. Rogl, X.-Q. Chen, R. T. Khan, H. Michor, G. Hilscher, E. Royanian, K. Kumagai, D. Z. Li, Y. Y. Li, R. Podloucky, and P. Rogl, Unconventional superconducting phase in the weakly correlated noncentrosymmetric Mo<sub>3</sub>Al<sub>2</sub>C compound, *Phys. Rev. B* **82**, 064511 (2010).
- [16] C. Q. Xu, B. Li, J. J. Feng, W. H. Jiao, Y. K. Li, S. W. Liu, Y. X. Zhou, R. Sankar, N. D. Zhigadlo, H. B. Wang, Z. D. Han, B. Qian, W. Ye, W. Zhou, T. Shiroka, P. K. Biswas, X. Xu, and Z. X. Shi, Two-gap superconductivity and topological surface states in TaOsSi, *Phys. Rev. B* **100**, 134503 (2019).
- [17] N. P. Butch, P. Syers, K. Kirshenbaum, A. P. Hope, and J. Paglione, Superconductivity in the topological semimetal YPtBi, *Phys. Rev. B* **84**, 220504(R) (2011).
- [18] S.-Y. Guan, P.-J. Chen, M.-W. Chu, R. Sankar, F. Chou, H.-T. Jeng, C.-S. Chang, and T.-M. Chuang, Superconducting topological surface states in the noncentrosymmetric bulk superconductor PbTaSe<sub>2</sub>, *Sci. Adv.* **2**, e1600894 (2016).
- [19] G. Bian, T.-R. Chang, R. Sankar, S.-Y. Xu, H. Zheng, T. Neupert, C.-K. Chiu, S.-M. Huang, G. Chang, I. Belopolski, D. S. Sanchez, M. Neupane, N. Alidoust, C. Liu, B. Wang, C.-C. Lee, H.-T. Jeng, C. Zhang, Z. Yuan, S. Jia *et al.*, Topological nodal-line fermions in spin-orbit metal PbTaSe<sub>2</sub>, *Nat. Commun.* **7**, 10556 (2016).
- [20] M. M. Sharma, L. Sang, P. Rani, X. L. Wang, and V. P. S. Awana, Bulk Superconductivity Below 6 K in PdBi<sub>2</sub>Te<sub>3</sub> Topological Single Crystal, *J. Supercond. Nov. Magn.* **33**, 1243 (2020).
- [21] H. Takeya, S. Kasahara, M. El Massalami, T. Mochiku, K. Hirata, and K. Togano, Physical Properties of Li<sub>2</sub>Pd<sub>3</sub>B and Li<sub>2</sub>Pt<sub>3</sub>B Superconductors, *Mater. Sci. For.* **561–565**, 2079 (2007).
- [22] P. Badica, T. Kondo, and K. Togano, Superconductivity in a New Pseudo-Binary Li<sub>2</sub>B(Pd<sub>1-x</sub>Pt<sub>x</sub>)<sub>3</sub> ( $x = 0 - 1$ ) Boride System, *J. Phys. Soc. Jpn.* **74**, 1014 (2005).
- [23] A. D. Hillier, J. Quintanilla, and R. Cywinski, Evidence for Time-Reversal Symmetry Breaking in the Noncentrosymmetric Superconductor LaNiC<sub>2</sub>, *Phys. Rev. Lett.* **102**, 117007 (2009).
- [24] B. Li, C. Q. Xu, W. Zhou, W. H. Jiao, R. Sankar, F. M. Zhang, H. H. Hou, X. F. Jiang, B. Qian, B. Chen, A. F. Bangura, and X. Xu, Evidence of s-wave superconductivity in the noncentrosymmetric La<sub>7</sub>Ir<sub>3</sub>, *Sci. Rep.* **8**, 651 (2018).
- [25] T. Shang, S. K. Ghosh, J. Z. Zhao, L.-J. Chang, C. Baines, M. K. Lee, D. J. Gawryluk, M. Shi, M. Medarde, J. Quintanilla, and T. Shiroka, Time-reversal symmetry breaking in the noncentrosymmetric Zr<sub>3</sub>Ir superconductor, *Phys. Rev. B* **102**, 020503(R) (2020).
- [26] S. Yashiro, A. Kasahi, R. Kasai, H. Samata, and Y. Nagata, New equiatomic silicides of MM'Si (M=Nb, Ta; M'=Pt, Rh) and superconductivity of Ta<sub>1-x</sub>Nb<sub>x</sub>PtSi, *J. Alloys Compd.* **309**, 51 (2000).

- [27] H. Su, T. Shang, F. Du, C. F. Chen, H. Q. Ye, X. Lu, C. Cao, M. Smidman, and H. Q. Yuan, NbReSi: A noncentrosymmetric superconductor with large upper critical field, *Phys. Rev. Mater.* **5**, 114802 (2021).
- [28] Sajilesh K. P., K. Motla, P. K. Meena, A. Kataria, C. Patra, S. K., A. D. Hillier, and R. P. Singh, Superconductivity in noncentrosymmetric NbReSi investigated by muon spin rotation and relaxation, *Phys. Rev. B* **105**, 094523 (2022).
- [29] T. Shang, D. Tay, H. Su, H. Q. Yuan, and T. Shiroka, Evidence of fully gapped superconductivity in NbReSi: A combined  $\mu$  SR and NMR study, *Phys. Rev. B* **105**, 144506 (2022).
- [30] S. K. P and R. P. Singh, Superconducting properties of the non-centrosymmetric superconductors TaXSi ( $X = \text{Re, Ru}$ ), *Supercond. Sci. Technol.* **34**, 055003 (2021).
- [31] See Supplemental Material at <http://link.aps.org/supplemental/10.1103/PhysRevB.107.134518> for the compositional analysis and the two-gap model fitting. See also Ref. [32] for two-gap model.
- [32] T. Charikova, N. Shelushinina, G. Harus, D. Petukhov, V. Neverov, and A. Ivanov, Upper critical field in electron-doped cuprate superconductor  $\text{Nd}_{2-x}\text{Ce}_x\text{CuO}_{4+\delta}$ : Two-gap model, *Phys. C: Supercond. Appl.* **488**, 25 (2013).
- [33] H. M. Rietveld, A profile refinement method for nuclear and magnetic structures, *J. Appl. Crystallogr.* **2**, 65 (1969).
- [34] M. Tinkham, *Introduction to superconductivity* (McGraw - Hill, New York, 2004), pp. 148–195.
- [35] M. A. Tanatar, N. Ni, C. Martin, R. T. Gordon, H. Kim, V. G. Kogan, G. D. Samolyuk, S. L. Bud'ko, P. C. Canfield, and R. Prozorov, Anisotropy of the iron pnictide superconductor  $\text{Ba}(\text{Fe}_{1-x}\text{Co}_x)_2\text{As}_2$  ( $x = 0.074$ ,  $T_c = 23$  K), *Phys. Rev. B* **79**, 094507 (2009).
- [36] C. P. Bean, Magnetization of High-Field Superconductors, *Rev. Mod. Phys.* **36**, 31 (1964).
- [37] B. I. Shklovskii and A. L. Efros, in *Electronic properties of doped semiconductors* (Springer Berlin, Heidelberg, 1984) pp. 202–227.
- [38] G. Xu, W. Wang, X. Zhang, Y. Du, E. Liu, S. Wang, G. Wu, Z. Liu, and X. X. Zhang, Weak Antilocalization Effect and Noncentrosymmetric Superconductivity in a Topologically Nontrivial Semimetal LuPdBi, *Sci. Rep.* **4**, 5709 (2014).
- [39] K. Gofryk, D. Kaczorowski, T. Plackowski, A. Leithe-Jasper, and Y. Grin, Magnetic and transport properties of rare-earth-based half-Heusler phases RPdBi: Prospective systems for topological quantum phenomena, *Phys. Rev. B* **84**, 035208 (2011).
- [40] N. Werthamer, E. Helfand, and P. Hohenberg, Temperature and Purity Dependence of the Superconducting Critical Field,  $H_{c2}$ . III. Electron Spin and Spin-Orbit Effects, *Phys. Rev.* **147**, 295 (1966).
- [41] D. Solenov, M. Nikolo, J. Singleton, J. Jiang, J. Weiss, and E. Hellstrom, The impact of Maki parameter and spin orbit scattering constant in the WHH model on upper critical magnetic fields in Ni- and co-doped pnictide bulk superconductors, *AIP Conf. Proc.* **1895**, 060004 (2017).
- [42] A. Abou El Hassan, A. Labrag, A. Taoufik, M. Bghour, H. El Ouaddi, A. Tirbiyine, B. Lmouden, A. Hafid, and H. El Hamidi, Magnetic Penetration Depth and Coherence Length in a Single-Crystal  $\text{YBa}_2\text{Cu}_3\text{O}_{7-\delta}$ , *Phys. Status Solidi B* **258**, 2100292 (2021).
- [43] J. R. Clem, Phenomenological theory of magnetic structure in the high-temperature superconductors, *Phys. C: Supercond. Appl.* **162–164**, 1137 (1989).